

# Correlative In Situ Multichannel Imaging for Large-Area Monitoring of Morphology Formation in Solution-Processed Perovskite Layers

Simon Ternes,\* Felix Laufer, Philip Scharfer, Wilhelm Schabel, Bryce S. Richards, Ian A. Howard, and Ulrich W. Paetzold\*

To scale up production of perovskite photovoltaics, state-of-the-art laboratory recipes and processes must be transferred to large-area coating and drying systems. The development of in situ monitoring methods that provide real-time feedback for process control is pivotal to overcome this challenge. Herein, correlative in situ multichannel imaging (IMI) obtaining reflectance, photoluminescence intensity, and central photoluminescence emission wavelength images on areas larger than 100 cm<sup>2</sup> with subsecond temporal resolution using a simple, cost-effective setup is demonstrated. Installed on top of a drying channel with controllable laminar air flow and substrate temperature, IMI is shown to consistently monitor solution film drying, perovskite nucleation, and perovskite crystallization. If the processing parameters differ, IMI reveals characteristic changes in large-area perovskite formation dynamics already before the final annealing step. Moreover, when IMI is used to study >130 blade-coated devices processed at the same parameters, about 90% of low-performing devices contain coating inhomogeneities detected by IMI. The results demonstrate that IMI should be of value for real-time 2D monitoring and feedback control in industrial-scale, high-throughput fabrication such as roll-to-roll printing.

## 1. Introduction

The unprecedentedly fast rise in power conversion efficiencies (PCEs) of perovskite solar cells (PSCs) over the last decade<sup>[1]</sup>—now surpassing 25%—triggered enormous scientific and industrial interest in solution-processed, large-area perovskite photovoltaics.<sup>[2]</sup> However, PCEs of PSCs and perovskite modules processed with scalable coating techniques lag behind solution-processed small-area PSCs.<sup>[3]</sup> The record certified PCE of a large, solution-processed perovskite module (802 cm<sup>2</sup>) of 17.9% was achieved by Panasonic.<sup>[4]</sup> Some of the losses on upscaling to modules originate from the monolithic interconnection schemes, including the sheet resistances of the transparent conductive oxides (TCOs), the series resistances of the TCO-Electrode interconnections, and the inactive areas due to the scribing lines.<sup>[5]</sup> A decrease in PCE of around 1.5%<sub>abs</sub> is typical for laser patterning of the three

scribe lines (p1, p2, p3), nearly independent on the module's aperture area.<sup>[6]</sup> However, just as in other researched thin-film photovoltaic (PV) technologies,<sup>[7]</sup> the dominant losses of PCE on large-area perovskite modules are caused by morphological defects in the absorber layer such as microcracks, material impurities, or, most commonly, shunt paths. Even one defect in the perovskite thin film can shunt a whole subcell or decrease its performance substantially by introducing nonradiative recombination.<sup>[6]</sup> These upscaling losses statistically increase with the modules' aperture area because the probability of defects scales with the area, limiting the achievable PCE of the whole module.<sup>[8]</sup>


The challenge of depositing homogeneous high-quality perovskite thin films on large areas arises from the complexity of the involved kinetic and thermodynamic processes.<sup>[9]</sup> In this work, we will focus on scalable perovskite processing from solution (although thermal coevaporation of the precursor materials<sup>[10]</sup> is a very promising fabrication route, as well). The reason for this focus is simply that the experimental techniques presented here are not yet adapted to operation in vacuum.

The formation of perovskite thin films from solution is commonly described via the following four stages:<sup>[3]</sup> I) coating—deposition of a wet film of precursor solution; II) drying—

S. Ternes, B. S. Richards, I. A. Howard, U. W. Paetzold  
Institute of Microstructure Technology  
Karlsruhe Institute of Technology  
Hermann-von-Helmholtz-Platz 1, 76344 Eggenstein-Leopoldshafen,  
Germany  
E-mail: simon.ternes@kit.edu; ulrich.paetzold@kit.edu

S. Ternes, F. Laufer, B. S. Richards, I. A. Howard, U. W. Paetzold  
Light Technology Institute  
Karlsruhe Institute of Technology  
Engesserstr. 13, 76131 Karlsruhe, Germany

S. Ternes, P. Scharfer, W. Schabel  
Thin Film Technology (TFT)  
Karlsruhe Institute of Technology  
Kaiserstr. 12, 76131 Karlsruhe, Germany

 The ORCID identification number(s) for the author(s) of this article can be found under <https://doi.org/10.1002/solr.202100353>.

© 2021 The Authors. Solar RRL published by Wiley-VCH GmbH. This is an open access article under the terms of the Creative Commons Attribution-NonCommercial License, which permits use, distribution and reproduction in any medium, provided the original work is properly cited and is not used for commercial purposes.

DOI: 10.1002/solr.202100353

solvent evaporation out of the wet film leaving behind a dry, amorphous film; III) nucleation—formation of crystalline seeds through supersaturation; and IV) (re-)crystallization—coalescence of crystalline colloids and formation of crystalline grains by crystal growth.

Several strategies involving antisolvent quenching,<sup>[11]</sup> gas quenching,<sup>[12]</sup> vacuum quenching,<sup>[13]</sup> and additives in the precursor solution<sup>[14]</sup> have demonstrated control of these stages for lab-scale devices. While these studies are certainly justified by significant advances in morphology control and thus the PSC device performances,<sup>[15]</sup> they often do not fully address the question how to transfer these processes to commercial-scale production lines. Furthermore, the understanding of these mechanisms relies heavily on ex situ investigation of the final polycrystalline perovskite morphology. For a successful scale-up, the discrimination, analysis, and control of the dynamic perovskite formation stages, I–IV, are important; each stage needs to be well controlled in a spatially uniform manner. For this purpose, in situ characterization methods capable of monitoring the perovskite formation in subsecond temporal resolution are needed. Preferably, such method should also have a large-area detection window with high spatial resolution to enable direct application in industrial-scale production lines.

In this context, several groups are working on in situ photon-in-photon-out characterization techniques (as described later) because these methods are noninvasive, have high sampling rates, and can operate in ambient environments. The techniques can be classified according to the wavelength range of the incident photons (probe). In situ X-ray diffraction<sup>[16–18]</sup> revealed important insight into the structural evolution of the perovskite lattice from the liquid solution. However, it would require great efforts to image large areas with X-ray scattering. These concerns also apply for certain techniques operating in the infrared (IR), such as Fourier transform infrared spectroscopy and terahertz spectroscopy that were performed in situ on perovskite thin films for finding *N,N*-dimethylformamide (DMF) and dimethyl sulfoxide (DMSO) containing intermediate phases<sup>[19,20]</sup> and resolving the crystal growth dynamics.<sup>[21]</sup> An example of large-area and fast imaging in the IR region is dark lock-in thermography<sup>[6]</sup> and simple thermography<sup>[22]</sup> that were, however, never demonstrated in situ to our knowledge. In the optical wavelength range, we distinguish between: 1) in situ absorption/reflection techniques probing the (wavelength dependent) absorption/reflection coefficients;<sup>[23–25]</sup> 2) in situ Raman spectroscopic techniques measuring the vibrational phonon–photon interactions of the material;<sup>[26]</sup> and 3) in situ luminescence techniques, detecting the light emitted by the radiative recombination of excited charge carriers.<sup>[23,27–30]</sup>

Optical (or IR) techniques have the advantages that they can be easily used for monitoring common solution processing methods such as spin coating<sup>[23,27,31]</sup> or blade coating<sup>[32,33]</sup> and that they can provide large-area information at low cost using cameras as imaging detectors, while the necessary large-area excitation can be provided by high-power light-emitting diodes. Luminescence and reflectance imaging on large areas—established already in other PV technologies as silicon,<sup>[34]</sup> GaAs,<sup>[35]</sup> CdTe,<sup>[36]</sup> and CIGS<sup>[37]</sup>—as well as luminescence microscopy<sup>[38,39]</sup> demonstrated to yield critical information on the perovskite thin-film quality and the performance of devices

incorporating these films.<sup>[40–44]</sup> However, to the best of our knowledge, there is currently no technique available combining both imaging capability on large areas and rapid real-time operation for analyzing the dynamics of the perovskite formation.

In response, we developed an in situ monitoring technique based on a commercially available scientific camera, an inexpensive ring light source, and a 3D printed rapidly rotating filter wheel that is able to generate sequences of images of reflectance, photoluminescence (PL) intensity, and an estimation of the central PL emission wavelength at a “frame-rate” of 3 fps each. This technique, which we call in situ multichannel imaging (IMI), enables the dynamic stages, I–IV, to be tracked in both space and time. To provide idealized conditions for testing the capability of IMI, we maintain full control of the air flow and temperature over the sample. With this idealized reference at hand, we will demonstrate that IMI would be useful in industrial-scale coating lines.

## 2. Results and Discussion

### 2.1. In Situ Multichannel Imaging for Perovskite Process Monitoring

IMI is a unique and scalable technique that is able to acquire reflectance, PL intensity, and PL emission wavelength images with high spatial and temporal resolution (experimental details about the setup are found in Experimental Section). Installed on top of a drying channel as shown in **Figure 1a**, IMI allows all the perovskite formation stages, I–IV, to be studied under well-defined reference conditions<sup>[45]</sup> (that is a laminar air flow and an exact substrate temperature). **Figure 1b–d** shows exemplary overviews of the data recorded by IMI through its reflectance, PL intensity, and central PL emission wavelength channels during the drying of a blade-coated perovskite precursor film (for details, see Experimental Section). Three images at the distinct times 10, 100, and 200 s are displayed along with four sample points, 1–4, in each image ( $t = 0$  s is chosen as the onset of the PL intensity upon nucleation). Below the images, the 1D transients extracted from the sample point positions are plotted with high temporal resolution.

For the application in a large roll-to-roll coating system, the IMI technique can be scaled by simply replicating the setup multiple times along the web and synchronizing the setups with a simultaneous trigger signal (see **Figure 1e**). High-throughput operation would be compatible with this configuration (for details, see Experimental Section). Yet, in the following analyses, we use a single IMI setup over a stationary substrate in the laminar flow channel as shown in **Figure 1a**. This configuration enables the assessment of the capabilities of IMI in a reference process of perovskite device fabrication by blade coating. It is crucial to note that this study demonstrates a correlation of the IMI data to the performances of the PCSs fabricated on the respective examined areas (for details, see Experimental Section). Based on this correlation or a similar study, IMI can be used in the future for in-line monitoring of a chosen solution process without the need to fabricate complete devices. For the assessment, we compare and correlate the IMI images and device performances of 20 blade-coated perovskite films (48 mm × 32 mm) dried in the

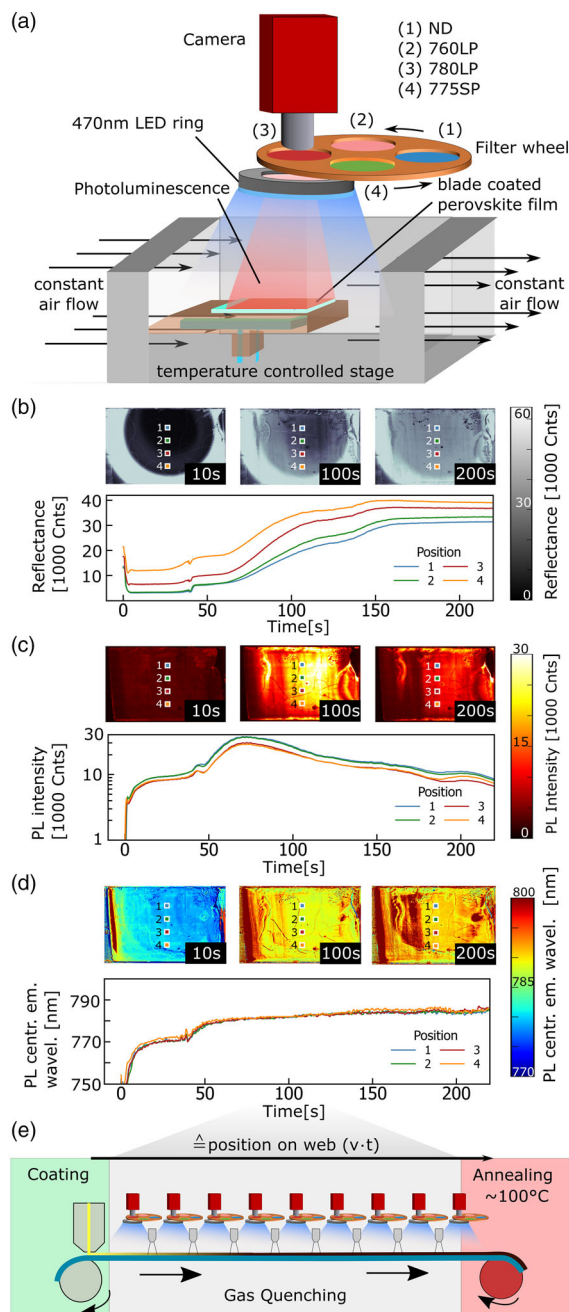


**Figure 1.** a) Schematic of the IMI setup mounted on top of a home-built drying channel for temperature and air flow control. The perovskite solution film is deposited by blade coating (omitted for simplification, details in Experimental Section). b) Reflectance, c) PL intensity, and d) PL central emission wavelength as measured over time (during the nucleation and recrystallization phases, III and IV) extracted from sample points drawn with corresponding colors in the exemplary full images taken at three instants in time. e) Schematic of a possible upscaled IMI technique in roll-to-roll fabrication by replication of the setup along the coating web. The employment of one setup in the drying channel on an evolving perovskite film as a function of time simulates data that many cameras would obtain on the roll at one instant in time as a function of the position on the web, given by the product of the web velocity  $v$  and time  $t$ .

laminar air flow at different processing parameters. Relying on an already optimized blade coating recipe of a previous work,<sup>[46]</sup> we compare IMI data of samples at different parameter regimes: three samples dried at a temperature of 30 °C and an air flow velocity of 0.02 m s<sup>-1</sup> (30 °C, 0.02 m s<sup>-1</sup>); three samples dried at a drying temperature of 20 °C and an air flow velocity of 2 m s<sup>-1</sup> (20 °C, 2 m s<sup>-1</sup>); and the remaining samples dried at a temperature of 40 °C and an air flow velocity of 2 m s<sup>-1</sup> (40 °C, 2 m s<sup>-1</sup>). The annealing temperature and time are kept constant at about 100 °C and 6 min (after a drying time of 3 min and a ramping time of 4 min), respectively. The results are summarized in Section 2.2 and **Figure 2a–d**, which are based on data available in the Full Videos in the Supporting Information. Subsequently, we demonstrate, by solely examining (40 °C, 2 m s<sup>-1</sup>) samples in more detail, that IMI is capable of detecting various types of coating defects in real-time during the perovskite formation process in Section 2.3 and **Figure 3**. We note that, although we use blade coating as reference coating method, IMI is also compatible to other scalable solution processing methods. In slot-die coating, the solution film is formed through a liquid meniscus such as in blade coating,<sup>[47]</sup> so no significant differences in the application constraints of IMI are expected (see again Figure 1e). In inkjet printing, the solution is deposited via a repetitive, fast ejection of small, individual droplets.<sup>[48]</sup> To apply IMI on such a system, one would need to make sure that the print head is not in the field of view, while it moves over the substrate. This could be achieved by synchronizing the camera trigger with the movement of the print head or by mounting IMI directly on top of the print head. The same constraints hold true for spray coating, where an (ultra-sonic) air nozzle ejects a mist of small droplets toward the substrate<sup>[49]</sup> (although such nozzle does not require very complex electronics and is therefore commonly smaller than an inkjet print head). To sum up, the only restriction for applying IMI to different coating methods is a free field of view on the drying thin film after the coating as measured from a minimal distance of 5 cm.

## 2.2. IMI Process Monitoring Comparison of Different Processing Conditions

Here, we demonstrate that IMI is able to consistently monitor solution film drying (stage II), perovskite nucleation (stage III), and perovskite (re-)crystallization (stage IV) over the entire sample area. If the processing parameters differ, IMI reveals characteristic transients in large-area perovskite formation dynamics already before the final annealing step, relying on its three input channels that are discussed in the following. We note that, for every processing parameter tuple, we have measured several substrates. The depicted 1D graphs in Figure 2 are thus a robust average over multiple substrates and multiple probing points, relying on 15 sample transients per parameter set.

### 2.2.1. Reflectance Channel

The drying of the coated perovskite solution film, stage II, is monitored in the reflectance channel (see Figure 2a,d and Full Videos with suffix “ND” in the Supporting Information) right after the blade passed through the field of view during coating,

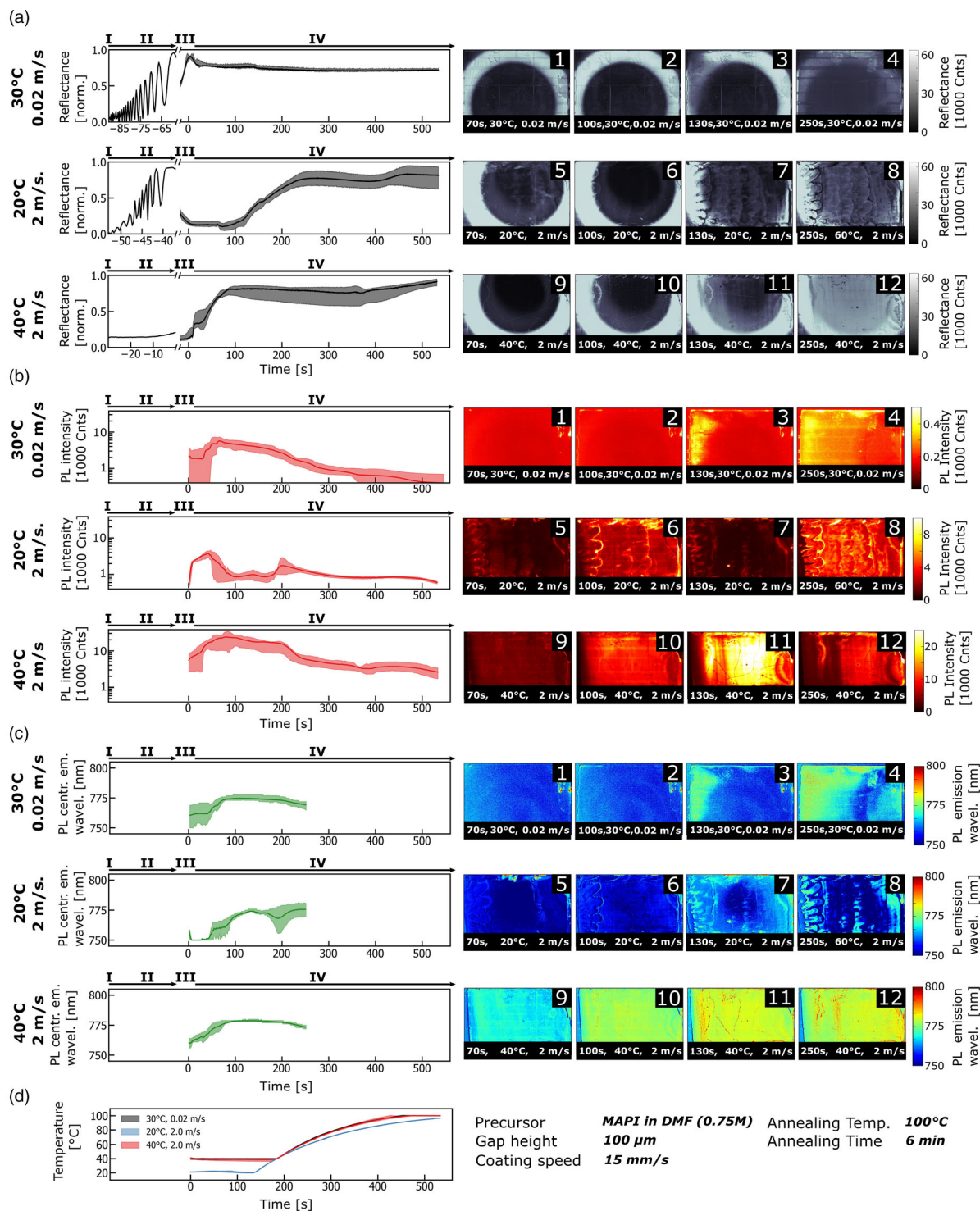


**Figure 2.** Comparison of in situ transients and sample images of the a) reflectance, b) PL intensity, and c) PL central emission wavelength channels along with the applied temperature and experimental parameters d) for three typical regimes: (30 °C, 0.02 m s<sup>-1</sup>), (20 °C, 2.0 m s<sup>-1</sup>), and (40 °C, 2.0 m s<sup>-1</sup>). The Full Videos can be downloaded from the Supporting Information. The solid line is the median over multiple points shifted in time with respect to the delay of the PL (and nucleation) onset,  $t = 0$  s, (see Figure S4, Supporting Information), while the shaded area is enclosed by the 75% and 25% quartiles. (In particular, the time in the labels of images 1–4, 5–8, and 9–12, which is the time starting with the coating stage I, is shifted 26.6, 10.4, and 8.1 s, respectively, relative to the time of the common x-axes). The perovskite formation stages, I–IV, are indicated on top of this data. The PL wavelength calculation was truncated at the point in time where the camera signal was of comparable magnitude as the camera’s noise level (measured on an image extract with no sample).

stage I. In this drying stage, the wet solution film is transparent, such that the surface of the patterned ITO/SnO<sub>2</sub> glass substrate is visible (see Figure 2a, Image 1 and/or Full Videos with suffix “ND”). On the samples fabricated at (30 °C, 0.02 m s<sup>-1</sup>) and at (20 °C, 2 m s<sup>-1</sup>), we observe oscillations in the reflectance channel for about 30 s (see 1D data marked with the drying stage II). These oscillations result from thin-film interference during solvent evaporation and correlate with the drying rate (see Suppl. Note 5 and Figure S5, Supporting Information). We note that the decreasing oscillation frequency/drying rate before the end of the drying process is in accordance with state-of-the-art modeling of the drying process in wet perovskite solution films.<sup>[46]</sup> For the (40 °C, 2 m s<sup>-1</sup>) samples, the drying process is so fast that the oscillations average out during the chosen 10 ms exposure time of the camera. However, for all investigated regimes, it is possible to compare the overall, average drying rates relative to each other: we assume that these rates are given by the same wet film thickness divided by the respective drying time—defined as the timespan from the coating, stage I, until the onset of the nucleation, stage III (the latter is detailed later). This assumption is valid considering the same blading speed, gap, and solution volume is used for all substrates and the fact that the viscosity<sup>[50]</sup> of the solution does not change much by temperature differences of only 10 K. The drying time results in around 10 s for the (40 °C, 2 m s<sup>-1</sup>) parameter samples, around 3 times as much for the (20 °C, 2 m s<sup>-1</sup>) samples and 8 times as much for the (30 °C, 0.02 m s<sup>-1</sup>) samples. It is evident that both the temperature and the air speed impact the drying rate (see additionally Figure S6a,b, Supporting Information). Moreover, we qualitatively assess the homogeneity of the transparent solution film because inhomogeneities at the surface of the solution thin-film deflect the light emitted by the LED ring. For example, in case of the (20 °C, 2 m s<sup>-1</sup>) sample, the solution is pushed in transparent droplets over the sample by the air flow (see Full Video “02\_low\_temperature\_ND”). This undesirable process is easily detected by monitoring the reflectance video, and could be used to adjust process parameters.

Subsequent to the drying, the reflectance decreases due to the formation of the perovskite absorber, indicating clearly the onset of the nucleation process, stage III (see Full Videos with suffix “ND”). This is marked as  $t = 0$  s on the graph and all 1D averaged transients in Figure 2 (as well as Figure 1) are shifted to this very same point in time. (Due to the asymmetry of the air flow, the nucleation starts at the left edge of the sample where the air flow arrives and moves to the right with time for all regimes.)

Differences in the homogeneity of the reflectance after the nucleation yield information about the nucleation density and the crystal growth. For samples deposited at (30 °C, 0.02 m s<sup>-1</sup>), the solution slowly transitions into the supersaturation. Therefore, the nucleation density is low and the growth of individual nuclei can be observed (see Figure 2a, Images 3–4 and Full Video “01\_low\_air\_flow\_ND”). As a consequence, the perovskite thin film appears very rough (root mean square roughness  $S_q = 0.43 \mu\text{m}$  measured by white-light interferometer [WLI]) and exhibits many areas where the perovskite does not cover the substrate, which is, in turn, detrimental for the device performances as detailed later. At (20 °C, 2 m s<sup>-1</sup>) and (40 °C, 2 m s<sup>-1</sup>) however, the reflectance image appears homogenous after the nucleation

because the nucleation density is higher than the spatial resolution of IMI, as caused by a rapid drying due to the high air flow (see Images 5–6 and 9–10 in Figure 2a and Full Videos “01\_low\_temperature\_ND” and “01\_optimal\_ND”). Under the (40 °C, 2 m s<sup>-1</sup>) regime, the perovskite film cracks into several segments (best visible in video “01\_optimal\_ND”). This is accounted to internal stress occurring upon the fast drying of the film.<sup>[51]</sup> (As the cracks are very narrow, we will classify them as thickness/roughness variations in Section 2.3).

Subsequent to the nucleation, the reflectivity of the film increases for the (20 °C, 2 m s<sup>-1</sup>) and (40 °C, 2 m s<sup>-1</sup>) parameter scenarios (see increasing reflectance in 1D plots in second and third row of Figure 2a, Images 7–8 and 11–12 as well as Full Videos “01\_low\_temperature\_ND” and “01\_optimal\_ND”). The reason is that the nucleated crystal grains coalesce as part of the (re)crystallization, stage IV, to yield a new surface with increased diffuse scattering from the surface. In the (40 °C, 2 m s<sup>-1</sup>) parameter regime, this coalescence occurs at about  $t = 100$  s, exhibiting a morphological landscape of connected crystalline segments as well as pinholes and coating inhomogeneities (Figure 2a, Image 12). These features and their effects will be further analyzed in Section 2.3. For the (20 °C, 2 m s<sup>-1</sup>) samples, the emerging surface is rougher (root mean square roughness  $S_q = 0.28 \mu\text{m}$  measured by WLI) than in the case of the (40 °C, 2 m s<sup>-1</sup>) samples (root mean square roughness  $S_q = 0.19 \mu\text{m}$  measured by WLI) as caused by the inhomogeneous wet film described earlier. For these samples, the coalescence occurs in two substages; a very short one at  $t = 105$  s (only visible in the Full Video “02\_low\_temperature\_ND”) and another one at  $t = 200$  s when the temperature is elevated to 50 °C (see second 1D plot of Figure 2a and Image 8). This dynamic is attributed to remaining volatile components in the film at  $T = 20^\circ\text{C}$  that partially delay the crystallization. These are, for example, methylammonium in compound with residual chloride and acetate trihydrate introduced by the lead salts<sup>[52,53]</sup> or simply H<sub>2</sub>O contained in the acetate trihydrate. For the (30 °C, 0.02 m s<sup>-1</sup>) samples, no coalescence is observed, which is once more an indication for rough, individual crystalline islands that leave uncovered areas in between (see Images 1–4 of Figure 2a and Full Video “01\_low\_air\_flow\_ND”). Consequently, for the (30 °C, 0.02 m s<sup>-1</sup>) samples, the reflectance signal remains almost on a constant level, only showing a very slight drift because the light is mainly reflected by the glass surface, while the perovskite crystals have a minor contribution (see reflectance in 1D plot in first row of Figure 2a). Altogether, our analyses show that IMI consistently monitors the speed of solution film drying, stage II, the reflectance decrease upon the nucleation, stage III, and inhomogeneities in the evolving polycrystalline perovskite thin-film morphology during the (re-)crystallization, stage IV.

### 2.2.2. PL Intensity Channel

For all investigated samples, the PL emerges with the onset of the nucleation process of the perovskite absorber, stage III. The perovskite nucleates first at the edge closest to the impinging air flow and then the nucleation front progresses from left to right along the air flow direction (as visible in Figure S4,

Supporting Information, Figure 2b, Images 1–4 and all the Full Videos with suffix “PL”). The time that the nucleation front needs to cross the 48 mm long substrate from the left to right depends on the drying parameters. Under the (30 °C, 0.02 m s<sup>-1</sup>) regime this time is around 220 s, for the (20 °C, 2 m s<sup>-1</sup>) regime around 50 s, and for the (40 °C, 2 m s<sup>-1</sup>) regime around 20 s. As explained earlier, in the 1D data shown in Figure 2 (and Figure 1), we compensate for this delay by shifting the transients to the initial onset of the PL intensity ( $t = 0$  s). (The data is then averaged over multiple spots on multiple samples and plotted as the median along with its 25% and 75% quartiles.)

Comparing the PL intensity in the (40 °C, 2 m s<sup>-1</sup>) parameter regime with the other two scenarios, we realize that the overall PL intensity is much higher in the (40 °C, 2 m s<sup>-1</sup>) case (see height of 1D transients and scale bars on the right-hand side in Figure 2b). At its peak, the PL intensity averages to about 20 000 counts over the sample area, which is about 40 times higher than at the peak of the (30 °C, 0.02 m s<sup>-1</sup>) samples (around 500 counts) and 4 times higher than for the (20 °C, 2 m s) samples (around 5000 counts). These large differences in magnitude imply differences in the optoelectronic performance of these layers. A lower PL intensity at equal excitation is commonly attributed to a decrease in PL quantum efficiency (PLQE). The reason could be increased nonradiative recombination at defect sites,<sup>[54]</sup> thus a decrease in the internal PLQE. However, it is also possible that the coupling of the excitation light into the film<sup>[55]</sup> or the outcoupling of the PL<sup>[56]</sup> is altered due to different optical properties of the film surface decreasing the external PLQE (as will be explained in the next section). In both cases, it is very likely that differences in the respective polycrystalline thin-film morphologies, that is, the texture and roughness, play a role. A closed film with large grains was demonstrated to yield higher PL intensities due to a lower nonradiative recombination probability at the SnO<sub>2</sub>/perovskite interface<sup>[57]</sup> or a lower density of grain boundaries<sup>[58]</sup> (although these results are still under discussion, to date<sup>[59]</sup>). However, it is certain that significant differences in thin-film morphology imply different coupling to excitation light and outcoupling in the direction of the detector, decreasing or increasing the external PLQE.<sup>[60]</sup> Consistently, the statistical distribution of the PCEs of PSCs incorporating the respective thin films shows significant differences in the optoelectrical performance depending on the processing conditions (see Figure S7, Supporting Information). For the (30 °C, 0.02 m s<sup>-1</sup>) samples, most device PCEs are around 5%, while it is about 10% for the (20 °C, 2 m s<sup>-1</sup>) and 15% for the (40 °C, 2 m s<sup>-1</sup>) samples. However, the statistical spread remains high for all scenarios, originating from random defects (further analyzed in Section 2.3).

The transient shape of the PL intensity over time can be explained as follows. In all three regimes, the PL intensity exhibits a broad maximum around 50–100 s after the nucleation onset (see 1D average data in all three rows Figure 2b). We conclude that the initial PL increase could be simply caused by more and more perovskite crystal seeds nucleating and growing in the supersaturated solution. This explanation is confirmed by extensive research of other groups.<sup>[52,61]</sup> In addition, it is plausible that the defect density decreases with the drying time increasing the PLQE, possibly due to the influence of humidity<sup>[28,62]</sup> or due to photocuring.<sup>[63]</sup> The subsequent decrease in PL intensity is

commonly attributed to structural changes within the perovskite as caused by the (re-)crystallization process, stage IV: Wagner et al. state that the merging of individual crystal seeds increases the nonradiative recombination probability due to the forming of new crystal boundaries favoring this energy transfer.<sup>[61]</sup> Franeker et al. attribute the decrease in the PL intensity to an increase in the diffusion length along the vertical direction of the film, enabling the charge carriers to recombine nonradiatively at the bottom contact.<sup>[23]</sup> Both of these mechanisms are highly plausible.

Under the (30 °C, 0.02 m s<sup>-1</sup>) and (40 °C, 2 m s<sup>-1</sup>) parameter regimes, the PL intensity decrease becomes steeper when the temperature of the substrate is ramped (compare the 1D transients in Figure 2b with Figure 2d). In case of the (20 °C, 2 m s<sup>-1</sup>) samples, the PL intensity exhibits a second maximum at  $T = 50$  °C, which coincides with the coalescence observed in the reflectance (probably caused by the removal of volatile residuals as described earlier). However, after this maximum, the PL intensity decay occurs just as in the other two scenarios. This further PL decrease is possibly associated with additional morphological changes but is certainly also caused by the increased rates of nonradiative recombination at elevated temperatures<sup>[64]</sup> (radiative recombination alone would show an opposite trend<sup>[65]</sup>). In addition, the excitation light might induce degradation,<sup>[66,67]</sup> which is evidently accelerated by elevated temperatures. In this context, it is reported that chemical reactions of the perovskite with oxygen and humidity may decrease the PL intensity.<sup>[52,68]</sup> This decay continues until the noise level of the IMI camera is reached given the limited power of the excitation light. Other groups report that the PL intensity continues decreasing until the end of the annealing process.<sup>[23,52]</sup>

In summary, with regard to the correlative in situ characterization of the perovskite thin-film formation process, we demonstrate that IMI consistently monitors perovskite nucleation and perovskite crystallization over the entire sample area. Moreover, IMI detects substantial differences between different process parameter regimes.

### 2.2.3. PL Central Emission Wavelength Channel

Next, we analyze the PL central emission wavelength (calculated as described later in Experimental Section and Suppl. Note 2), which is a characteristic indicator of the perovskite band structure. The emission starts at about 760 nm and then converges toward about 780 nm for all processed regimes (see 1D average data Figure 2c, Figure 2d and Full Videos with suffix “EG”). Consequently, a redshift in the central emission wavelength of about 20 nm is observed. A very similar redshift was reported before by in situ single spot PL analyses of drying perovskite wet films and attributed to the growth and coalescence of perovskite crystalline grains.<sup>[52,61]</sup> (We note that, here, we show for the first time the spatial imaging of this phenomenon over the entire substrate and use it for correlative analysis.) Agreement with this explanation can be found in reports, stating that the PL peak position depends on the average crystal grain size present in a perovskite thin film,<sup>[27,61,69,70]</sup> which could be partially caused by quantum confinement of excited charges in crystal domains with comparable size as their exciton Bohr radius

(<25 nm).<sup>[71]</sup> Other effects contributing to the redshift are, first, the growing film thickness increasing the average pathlength of photons before emission, thereby increasing the probability for photons to be reabsorbed and reemitted with lower energy.<sup>[56]</sup> Second, it is possible that the outcoupling probability of “red,” below-bandgap photons that were initially trapped in the film increases due to increasing surface roughness.<sup>[56]</sup> Finally, perovskite thin films dried under humid conditions were shown to exhibit a redshift of about 20 nm.<sup>[28]</sup> All these explanations are consistent with the fact that the redshift occurs simultaneously with an increasing PL intensity during nucleation and seed growth, the onset of stage III, as explained earlier.

The homogeneity of the central PL emission wavelength after the initial redshift is an indicator of the quality of the formed film surface. For the (40 °C, 2 m s<sup>-1</sup>) samples, the wavelength converges to a constant value over the entire substrate area after about 100 s, only disturbed by individual defects which will be analyzed in detail in Section 2.3 (see Images 9–12 in Figure 2c and Full Video “03\_optimal\_EG”). Accordingly, the interquartile range (and thus the standard deviation) of the central PL emission wavelength transients is low compared with the other two regimes (see shaded areas in the 1D data in all rows in Figure 2c). The reasons for the deviations in these samples are explained in the following.

For the (30 °C, 0.02 m s<sup>-1</sup>) samples, the wavelength reaches about 790 nm in the left part on the substrate, while the right part of the substrate exhibits an opposite drift (see Images 3–4 in Figure 2c and Full Video “03\_low\_air\_flow\_EG”). This opposite drift indicates that the perovskite formation is not completed yet in this region. Furthermore, due to the lack of coalescence, the peak wavelength exhibits significant variations within the individual crystal grains, which is an indication for a poor optoelectronic performance consistent with the inferior device performances (see Figure S7, Supporting Information). For the (20 °C, 2 m s<sup>-1</sup>) samples, we find two plateaus that can be correlated with the temporal positions of the two maxima in the PL intensity due to the delayed formation dynamics described earlier (see 1D data in second row in Figure 2c and Full Video “03\_low\_temperature\_EG”). The first plateau in the wavelength range 750 to 760 nm is reached directly after the onset of the nucleation process. This is the spectral classification of the first PL intensity peak. Then, for most positions on the substrate, the emission shifts slowly toward 775 nm, the second plateau, until the temperature increases. Subsequently, the wavelength drops again and exhibits a minimum at the position of the second PL intensity peak. We hypothesize that, upon the first plateau, the growth and linking of nuclei reaches a semistable configuration, which is again altered with time until the final morphology is reached when the temperature is increased to 50 °C. As detailed earlier, the size and linking of crystallites influence the spectral characteristic of the thin film. Compared with the (40 °C, 2 m s<sup>-1</sup>) parameter samples, the wavelength images of the (20 °C, 2 m s<sup>-1</sup>) samples show very rough structures as caused by inhomogeneous coating due to the thickness and roughness dependence of the PL<sup>[56]</sup> (see Images 7–8 in Figure 2c and Full Video “3\_low\_temperature\_EG”). These coating inhomogeneities deteriorate the optoelectronic properties of these samples as compared with the ones processed in the (40 °C, 2 m s<sup>-1</sup>) regime (see PSC device performances in Figure S7, Supporting Information). For

all sample types, the PL intensity signal reaches the same magnitude as the noise level of the camera shortly after the temperature rises. At this position, the wavelength calculation method is not reliable anymore and the data are truncated at this point (compare 1D data in Figure 2b,c). Altogether, we demonstrate consistent measurements of the central PL emission wavelengths as they shift during the formation of the polycrystalline thin-film morphology—for the first time to our knowledge in high spatial and temporal resolution simultaneously.

#### 2.2.4. IMI for Direct Feedback Control

As shown in the preceding sections, the three image transients—recorded by IMI already before the annealing process—respond sensitively to differences in the processing parameters, air flow velocity, and temperature. Furthermore, IMI monitoring provides a high temporal resolution with large-area detection. These unique capabilities (combined with the ability to classify and localize defects described in Section 2.3) can be utilized to feed IMI data directly into control electronics connected to drying and coating machines, which is a prerequisite for establishing direct feedback control loops in perovskite deposition lines. Such direct feedback could be the essential stepping stone to control and reproduce perovskite deposition on large scales where the exact processing parameters can drift or there are unknown parameters such as ambient humidity, impurity of precursor materials, or coordination chemistry in the solution<sup>[72]</sup> affecting reproducibility. In this way, IMI would be a powerful tool for stabilizing the perovskite fabrication process on areas greater than 100 cm<sup>2</sup> (or even on larger areas and in high-throughput production using multiple setups, as shown in Figure 1e).

### 2.3. Predicting Device Failures with IMI

In Section 2.2, we demonstrated that, using correlative in situ characterization via IMI, we are able to distinguish different processing conditions based on differences in the recorded, average IMI transients and different macroscopic features in the large-area IMI images. In this section, we use IMI to monitor six substrates, later used for fabrication of 132 n-i-p architecture solar cells (not all substrates were used for this study), processed under the same (40 °C, 2 m s<sup>-1</sup>) parameter regime. In this way, we demonstrate that IMI is able to identify defects that appear randomly for this parameter regime.

#### 2.3.1. Correlative Localization of Inhomogeneities

We use IMI to obtain a multichannel image database tagged with the device performances by locating the active areas of the solar cells in the acquired images of the perovskite layer (the data acquisition is detailed later in Experimental Section). This spatially resolved data enable a correlative analysis encompassing the reflectance, the central PL emission wavelength, and PL intensity images on the in situ side, as well as the same images on the ex situ side, combined with an additional ex situ 2D film thickness profile image as recorded by the WLI for checking the consistency of our IMI data. (As detailed in Experimental Section later, we designate any data acquired after the end of the

annealing process at room temperature as ex situ). We investigate the in situ images at the instant of highest PL intensity along with the ex situ images and the WLI image as a demonstrative example (see Figure 3). Typical reverse  $J-V$  scans of the fabricated PSCs measured under the solar simulator are plotted (Figure 3d bottom) in correspondence with the magnified image extracts. We recognize clear correlations between the device performance and the recorded image extracts at the active areas of the PSCs. The colored rectangles indicate the positions of the active areas of the PSCs before the fabrication sequence is completed (see Experimental Section for detailed fabrication

sequence). The magnified images highlight the different types of inhomogeneities that can be detected with our IMI technique along with an extract where no defect is detected. The color code designates the category of the detected defect as explained in the next section.

### 2.3.2. Classification of Inhomogeneities

We identify three distinct categories of coating inhomogeneities that can be detected with IMI as shown in Figure 3, summarized in Table 1, and defined as follows: minor thickness/roughness

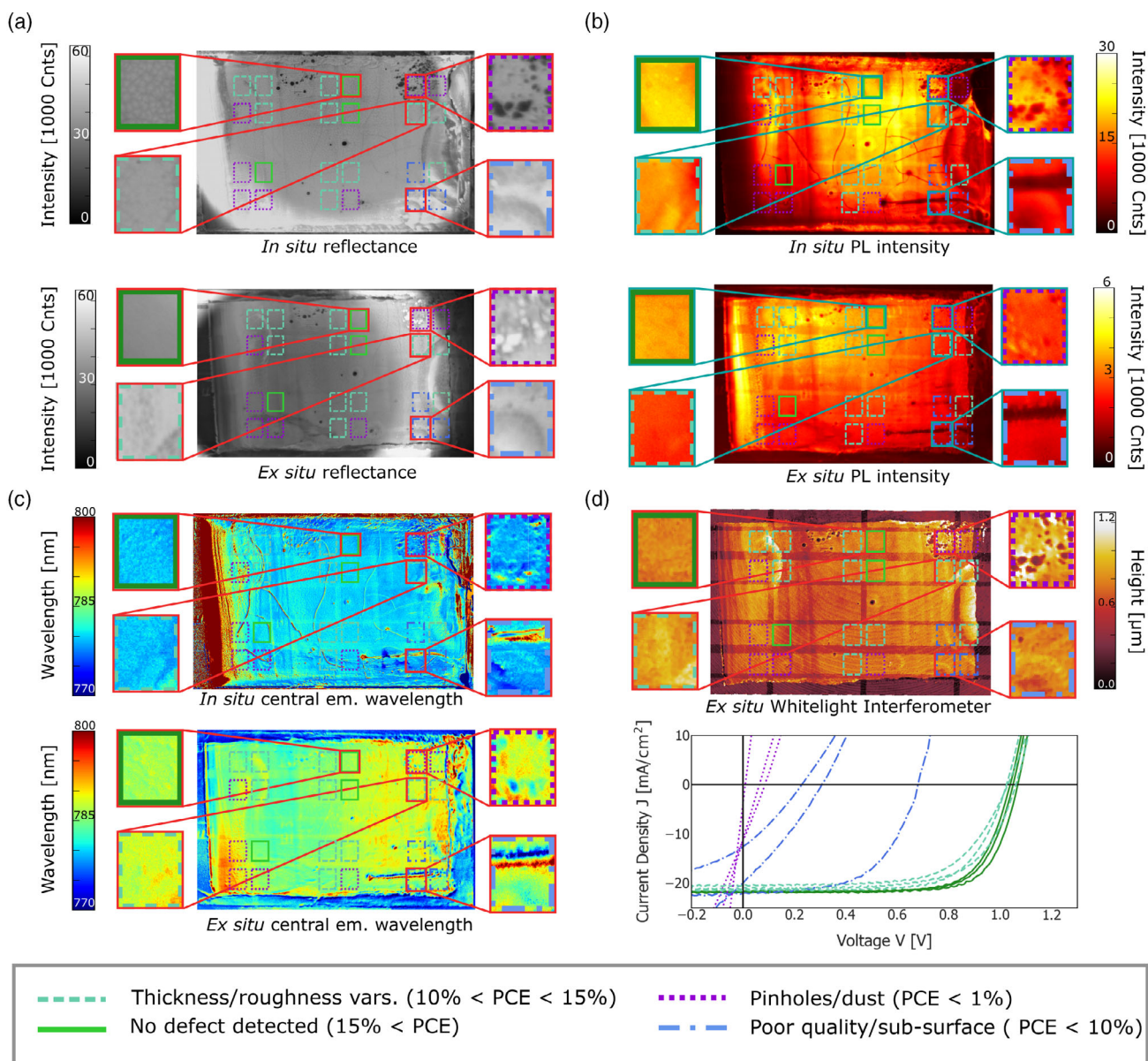


**Figure 3.** Detailed correlative analysis on one ( $40\text{ }^{\circ}\text{C}$ ,  $2\text{ ms}^{-1}$ ) sample, displaying in situ and ex situ a) reflectance, b) PL intensity, c) central PL emission wavelength images along with an ex situ d, top) WLI image, indicating the active areas of the solar cells fabricated later by color-coded rectangles. (No defect detected: solid green; thickness/roughness variations: dashed turquoise; semiconductor quality defects/subsurface defects: dash dotted blue, pinholes/dust-dotted purple) along with typical  $J-V$  curves of the solar cells incorporating the perovskite active areas of these categories (d, bottom). The in situ images were captured at a working distance of 150 mm, while the ex situ images were captured at 50 mm. (The reason is that in the ex situ case we do not utilize the drying channel).



**Table 1.** Classification of detected inhomogeneities/defects as detected by IMI in situ and ex situ mode as well as WLI (for the original data this table is based on, see Figures S8a,b, Supporting Information). The data are correlated with the device performances of the 132 n-i-p solar cells.

Source	Category I	Category II	Category III	No defect detected
	Thickness/roughness variations	Absorber quality/defect under surface	Pinholes/dust	Unknown
Best detection	In situ and ex situ PL, WLI	In situ and ex situ PL, emission wavelength	All channels, preferably ND, WLI	None
Impact	FF, $R_{series}$	$V_{OC}$ , FF, $R_{series}$ , $R_{shunt}$	FF, $V_{OC}$ , $J_{SC}$ , $R_{shunt}$	–
Performance of most devices	10% < PCE < 15%	PCE < 10%	PCE < 1% or n.a.	15% < PCE
#times detected (#times detected/#samples)	53 (40%)	12 (9%)	43 (33%)	24 (18%)
#devices with PCE < 10% in this category	24	10	43	9
#devices PCE < 10%/#times detected	45%	83%	100%	38%

variations indicated by lower and inhomogeneous in situ and ex situ PL intensity and emission wavelength, confirmed by ex situ WLI profile images (category I); semiconductor quality defects/subsurface defects indicated by dark spots of quenched in situ and ex situ PL intensity, accompanied by a fluctuating, unsteady in situ and ex situ PL emission wavelength but not visible in the WLI and reflection images (category II); as well as severe pinholes/defects visible in all image channels (category III). Regarding the classification, we conclude that PL imaging resolves about 10% more defects than pure reflection or WLI imaging, underlining the importance of the addition of PL imaging channels to in situ monitoring setups (see category II in Table 1). However, we note that reflectance imaging still identifies surprisingly many defects as simple morphological features (as well as other features as we showed in Section 2.2.1), which is why we included the reflectance in this work.

Importantly, we find that all defects observable in the ex situ (postanneal) PL can already be spotted before the annealing process in the in situ images. In fact, the defects are even more pronounced and easily observable in the preannealing in situ images. Combined with the advantage of rapid in situ monitoring to create feedback control mentioned earlier, this is clear indication that IMI is highly attractive in industrial production lines, especially when combined with other future extensions such as automated image analysis.

### 2.3.3. Correlating Detected Defects with Device Performance

In Table 1, a statistical analysis encompassing all investigated PSC active areas is presented, dividing them into groups according to the category of defect detected by IMI. The full, detailed statistical data are found in Figure S8a,b, Supporting Information. A defect detected by IMI during the film formation in an active area will, in average, lead to a poorer performing PSC. Thickness variations (category I) mostly decrease the FF and increase  $R_{series}$  due to insufficient or inhomogeneous diffusion of excited charge carriers. Quality variations indicated by quenched PL (category II) result in a considerably lower  $V_{OC}$ , as well as a higher  $R_{series}$  and lower FF due to increased nonradiative recombination. Pinholes (category III) decrease all  $J$ - $V$  parameters, and thereby inhibit a decent device performance. Pinholes cause shunts as indicated by a strongly decreased

$R_{shunt}$ , while  $R_{series}$  stays as low as in the case where no defects are detected.

Categories II and III affect the device performances more severely than category I. Out of all devices where the respective defect was detected, 100% performed under 10% PCE in category III, while 86% performed equally low in category II. In category I however, this fraction was only 45%. These numbers can be summarized to a remarkable result: out of the 86 low-performing PSCs (PCE < 10%) only 9 did not show any irregularities in the IMI images, proving that IMI is an effective tool for finding potentially flawed device areas. However, the IMI technique also detects many irregularities, which do not decrease the device PCE to a level under 10% (24% of total investigated devices). A future, more detailed image data analysis could tackle this “false positive” rate, providing a more detailed classification of defects based on their shape and temporal evolution to obtain a fine-grained PCE prediction. In addition, determining (or even imaging) the excited charge carrier lifetimes in the vicinity of these defects could be of great value for understanding their respective impact on the device PCEs. Given that the performance of a PSC reflects also on the quality of the layers deposited subsequent to the perovskite layer as well as the handling of the sample, it is obvious that not every failure of a PSC can be predicted by IMI. For this reason, about one-third of the PSCs (38%) built on active areas with no detected defect exhibit a performance under 10% PCE. This fundamental limitation can only be overcome by monitoring additionally the fabrication of the previous and/or subsequent layers, which could, in principle, be done by IMI in future works—possibly using an UV excitation to achieve photon energies above the bandgap of these layers. It remains, however, an open question if the PLQE of these layers would be high enough to measure their luminescence or if absorption/reflection would rather be the only available information.

## 3. Conclusion

Correlative IMI of perovskite films from the coating until the start of the annealing process is highly suitable for providing process feedback and in-line monitoring of large-area perovskite deposition processes. Detection of reflectance, PL intensity, and PL central emission wavelength images of high spatial

resolution on areas greater 100 cm<sup>2</sup> with subsecond temporal resolution allow differences in the process parameters to be identified. The characteristic transients in reflection, the PL intensity, and PL central emission wavelength can be used for feedback control in industrial processing machines because they allow slight parameter differences to be identified rapidly from IMI transient data. Direct feedback could be a fundamental necessity for controlling and reproducing the perovskite deposition on large areas and time scales, potentially saving substantial efforts in work time and material cost.

Furthermore, our first implementation of IMI performs very well in identifying the vast majority ( $\approx 90\%$ ) of random defects in the perovskite layer that will lead to poor cells (PCE obtained by reverse  $J$ - $V$  sweep smaller than 10%), even before the perovskite annealing step. This defect detection could be applied as an additional parameter for direct feedback control. Paired with the fact that the IMI technique is comparably cheap, minimally invasive, and scalable, IMI is well suited to industrial high-throughput applications such as roll-to-roll printing. It could help monitoring the perovskite deposition by providing early, direct feedback as well as assessing and localizing inhomogeneities to sort out scrap parts, all without the need to wait until the end of the annealing process. With more sophisticated analysis of IMI transient images, it could even become possible to precisely predict the local PCE values in the future.

## 4. Experimental Section

**IMI Setup:** The IMI setup consists of a scientific CMOS camera synchronized with a filter wheel rotating at a speed of 180 rpm and a 470 nm light-emitting diode ring for excitation (the precise part specifications can be found in Suppl. Note 1). Figure 1a shows a conceptual graphic of IMI, while Figure S1, Supporting Information, provides a schematic of the electronics and a labelled photograph of the setup. The resulting framerate is 3 fps per channel, while the camera operates at 12 fps with a 10 ms exposure time and a resolution of about 1000 pixels  $\times$  800 pixels. The four channels in the filter wheel are loaded with: 1) a neutral density filter with adjustable absorption (ND), 2 and 3) longpass filters at 760 and 780 nm (760LP and 780LP), respectively, and (4) a shortpass filter at 775 nm (775SP), combined with a 665 nm longpass filter to block the reflected excitation light that would be able to pass through the 775SP filter otherwise. An image is taken through each filter position in the wheel every time it rotates past the camera. First, the intensity of the reflected excitation light is imaged through the ND filter (see Figure 1b). Second, the PL intensity is calculated by the sum of the 780LP and the 775SP images (see Figure 1c). Third, the central PL emission wavelength is approximated based on the ratios of the 760LP, 780LP, and 775SP images (see Figure 1d). This is achieved using two look-up tables based on a simple optical model of perovskite PL emission spectra as introduced by Chen et al.<sup>[73]</sup> (for more detail, see Suppl. Note 2 and Figures S2–S3, Supporting Information).

We note that the excitation intensity was chosen as the maximum power of the provided LED ring (electrical power 23 W) because the PLQE was shown to increase with increasing excitation intensity before it saturates.<sup>[74]</sup> We measured the irradiation intensity at the working distance of 15 cm (same as in the setup shown in Figure 1a) from the LED ring with a Thorlabs S314C—Thermal Power Sensor Head (diameter 25 mm) yielding around 6 mW cm<sup>-2</sup> or 0.06 suns equivalent, which is still in the intensity range wherein the PLQE is expected to increase monotonously with excitation intensity.<sup>[74]</sup>

**Fabrication of Perovskite Solar Cells in the Drying Channel:** The IMI setup as described earlier is mounted directly onto the drying channel as visible in Figure 1a. To fabricate the half-stack PSCs, prepatterned 64  $\times$  64 mm<sup>2</sup>

ITO substrates (Luminescence Technology, sheet resistance 15  $\Omega$  sq<sup>-1</sup>, cleaned in an ultrasonic bath and with acetone/isopropanol and etched in an O<sub>2</sub>-plasma for 3 min) are spin-coated with SnO<sub>2</sub> nanoparticles colloidal dispersion (Alfa Aesar, 15%) diluted to a concentration of 2% (4000 rpm for 30 s with the initial volume of 400  $\mu$ L per substrate) and annealed at 250 °C for 60 min. Each such substrate is broken into two 32  $\times$  48 mm<sup>2</sup> substrates and again etched with O<sub>2</sub> plasma at 30% of the available power for 1 min. The substrates are placed on a copper plate inside of the drying channel on top of a TRU COMPONENTS TEC1-127145 Peltier-Element module controlled by a TEC16-24 High Power TEC Driver by head electronic. The bottom side of the Peltier module is placed on the drying channel's temperature stabilized table. A Zehntner, ZUA 2000 Universal Applicator is attached to a stepper motor with an adjusted gap of 100  $\mu$ m over the substrate. The selected perovskite precursor system is 0.75 M methylammonium lead iodide (MAPI) dissolved in *N,N*-dimethylformamide (DMF) with a mixture of 20% lead chloride and 80% lead acetate trihydrate and the fixed molar ratio MAI to Pb of 3:1. (PbCl<sub>2</sub>:3CH<sub>3</sub>NH<sub>3</sub>I is added to Pb(CH<sub>3</sub>COO)<sub>2</sub> · 3H<sub>2</sub>O:3CH<sub>3</sub>NH<sub>3</sub>I solution (DMF) such that PbCl<sub>2</sub>:Pb(CH<sub>3</sub>COO)<sub>2</sub> · 3H<sub>2</sub>O = 1:4 and the lead concentration is 0.75 mmol Pb per mL DMF). After the respective processing parameters are set, the solution is injected to form a meniscus and the blade is dragged over the substrate with the velocity of 15 mm s<sup>-1</sup>. The recording of the IMI system is started simultaneously with the coating process. After a drying time of 3 min, the TEC16-24 High Power TEC is set to the temperature 100 °C, slowly ramping up and stabilizing temperature within the annealing time of 6 min (and 4 min ramping time). The so-obtained substrates are scratched at the edges with a gamma-butyrolactone-soaked Q-tip obtaining an about 3 mm-thick frame. This frame is needed as a reference surface for the WLI measurement that is conducted right after. Furthermore, the IMI setup is used ex situ (that is after the annealing at room temperature) on the fabricated substrates at the shortest possible excitation and working distance of about 5 cm.

As a subsequent step, each substrate is broken into six 16  $\times$  16 mm<sup>2</sup> substrates and the Spiro-MeOTAD solution (80 mg Spiro-MeOTAD purchased by Luminescence Technology dissolved in 1 mL chlorobenzene doped with 28.5  $\mu$ L mL<sup>-1</sup> of 4-tert-butylpyridine and with 17.5  $\mu$ L of lithium bis(trifluoromethanesulfonyl) imide of a solution of 520 mg mL<sup>-1</sup> in acetonitrile) is spin-coated individually with 4000 rpm for 30 s on the 16  $\times$  16 mm<sup>2</sup> substrates. The Spiro layers are doped with oxygen under 12–15 h of air exposure (approx. 30% humidity). Eventually, the 75 nm-thick Au electrodes are evaporated with a shadow mask in a Vactec Coat 320 thermal evaporator, yielding four individual 0.105 cm<sup>2</sup> solar cells per substrate.

**Scale-Up of the IMI Technique:** For an implementation of IMI in a large-scale fabrication line, we consider the setup depicted in Figure 1e where IMI is replicated and synchronized along the web direction. Assuming that one camera has a field of view of 10 cm in web direction and using ten cameras, one can operate the line at web speeds up to 10 m min<sup>-1</sup> and still get 18 images of each position at different times in all channels (IMI has 3 fps per channel). Moreover, 10 m min<sup>-1</sup> is the upper boundary compatible with the exposure time of 1 ms of each camera, producing a blur below 1.7 pixels with a sensor width of 1000 pixels/10 cm. For the experiments introduced in the preceding section and discussed in the Section 2.2, we use 10 ms exposure time to increase the sensitivity of the IMI technique. However, considering the high signal strength of the sample fabricated at (40 °C, 2 m s<sup>-1</sup>) processing conditions in Figure 2b, 1 ms will be sufficient. By increasing the excitation light intensity and thereby the PL intensity even shorter exposure times could be used.

After a correction of the translation of subsequent images due to the web movement, one would obtain the reflectance, the PL intensity, and the PL central emission wavelength, calculated just as described earlier, as a function of the position along the movement direction of the web. These transients over the web movement position can be mapped to the transients over time we recorded in the drying channel with a single IMI setup as explained earlier, simply because the web moves with constant velocity,  $v$ . This highlights the relevance of the reference experiments introduced in the preceding sections for the industrial applicability of IMI. (Depending

on the web with another parallel row of cameras can be used to resolve the full direction orthogonal to the movement).

**Extensive Correlative Assessment of IMI:** As explained in Section 2.3, subsequent to the coating and annealing within the flow channel monitored by IMI, the substrates are further ex situ characterized by a large-area white-light interferometer (WLI, ISRA vision, NetGAGE3D-I) and by an ex situ close-up PL image acquired with the same IMI setup. Thereafter, the 48 mm × 32 mm substrates are used for the fabrication of 24 PSCs, as described earlier. (We present a large-area monitoring technique herein, but the probing devices are small-scale to achieve high sample numbers for the following statistical analyses.) The PCE of each PSC is determined by a reverse  $J$ - $V$  sweep (starting from 1.2 V back to  $-0.2$  V with  $1 \text{ V s}^{-1}$ ) under standard test conditions using a class AAA xenon-lamp-based solar simulator (Newport Oriel Sol3A). The resulting PCE,  $J_{\text{SC}}$ ,  $V_{\text{OC}}$ , and FF values as obtained by the reverse  $J$ - $V$  sweep are collected in a database along with the extracted, correlative images located at the active area of the respective cell. In addition, the series and shunt resistances,  $R_{\text{Series}}$  and  $R_{\text{Shunt}}$ , are calculated by a linear fit of the  $J$ - $V$  curves close to the  $V_{\text{OC}}$  and  $J_{\text{SC}}$ , respectively. (We are aware that the true PCE under constant voltage operation is systematically lower due to hysteresis and stability issues. We, however, want to point out that the absolute values are of less interest in the following analyses. Instead, we use the reverse  $J$ - $V$  sweep as a quick, rough determination of an upper boundary of the achievable PCE, which is sufficient to compare the PCEs of different PSCs relative to each other.)

## Supporting Information

Supporting Information is available from the Wiley Online Library or from the author.

## Acknowledgements

S.T. and F.L. contributed equally to this work. The authors gratefully acknowledge financial support of the German Federal Ministry of Education and Research (PRINTPERO, funding code: 03SF0557A), the Initiating and Networking funding of the Helmholtz Association (HYIG of U.W.P. (funding code: VH-NG1148); Recruitment Initiative of B.S.R.; the Helmholtz Energy Materials Foundry (HEMF); PEROSEED (funding code: ZT-0024); and Research Field Energy—Program Materials and Technologies for the Energy Transition—Topic 1 Photovoltaics), and the Karlsruhe School of Optics & Photonics (KSOP). The authors would like to thank the whole “perovskite task force” at KIT.

Open access funding enabled and organized by Projekt DEAL.

## Conflict of Interest

The authors declare no conflict of interest.

## Data Availability Statement

Research data are not shared.

## Keywords

correlative imaging, in situ, large-area, monitoring, perovskites, photoluminescence

Received: June 22, 2021

Revised: August 13, 2021

Published online:

- [1] NREL National Renewable Energy Laboratory, “NREL Efficiency chart,” 2021, <https://www.nrel.gov/pv/cell-efficiency.html> (accessed: June 2021).
- [2] Z. Li, T. R. Klein, D. H. Kim, M. Yang, J. J. Berry, M. F. A. M. van Hest, K. Zhu, *Nat. Rev. Mater.* **2018**, 3, 18017.
- [3] I. A. Howard, T. Abzieher, I. M. Hossain, H. Eggers, F. Schackmar, S. Ternes, B. S. Richards, U. Lemmer, U. W. Paetzold, *Adv. Mater.* **2019**, 31, 1806702.
- [4] M. A. Green, E. D. Dunlop, J. Hohl-Ebinger, M. Yoshita, N. Kopidakis, X. Hao, *Prog. Photovolt. Res. Appl.* **2020**, 28, 629.
- [5] Y. Galagan, E. W. C. Coenen, W. J. H. Verhees, R. Andriessen, *J. Mater. Chem. A* **2016**, 4, 5700.
- [6] L. Rakocevic, L. E. Mundt, R. Gehlhaar, T. Merckx, T. Aernouts, M. C. Schubert, S. W. Glunz, J. Poortmans, *Sol. RRL* **2019**, 3, 1900338.
- [7] R. Ebner, B. Kubicek, G. Újvári, S. Novalin, M. Rennhofer, M. Halwachs, *Int. J. Photoenergy* **2015**, 2015, 159458.
- [8] S. Dongaonkar, S. Loser, E. J. Sheets, K. Zaunbrecher, R. Agrawal, T. J. Marks, M. A. Alam, *Energy Environ. Sci.* **2013**, 6, 782.
- [9] S. T. Williams, A. Rajagopal, C. C. Chueh, A. K. Y. Jen, *J. Phys. Chem. Lett.* **2016**, 7, 811.
- [10] Y. Vaynzof, *Adv. Energy Mater.* **2020**, 10, 2003073.
- [11] S. Gharibzadeh, I. M. Hossain, P. Fassel, B. A. Nejjand, T. Abzieher, M. Schultes, E. Ahlswede, P. Jackson, M. Powalla, S. Schäfer, M. Rienacker, T. Wietler, R. Peibst, U. Lemmer, B. S. Richards, U. W. Paetzold, *Adv. Funct. Mater.* **2020**, 30, 1909919.
- [12] A. Babayigit, J. D’Haen, H. G. Boyen, B. Conings, *Joule* **2018**, 2, 1205.
- [13] F. Schackmar, H. Eggers, M. Frericks, B. S. Richards, U. Lemmer, G. Hernandez-Sosa, U. W. Paetzold, *Adv. Mater. Technol.* **2021**, 6, 2000271.
- [14] W. Qiu, T. Merckx, M. Jaysankar, C. Masse De La Huerta, L. Rakocevic, W. Zhang, U. W. Paetzold, R. Gehlhaar, L. Froyen, J. Poortmans, D. Cheyons, H. J. Snaith, P. Heremans, *Energy Environ. Sci.* **2016**, 9, 484.
- [15] I. A. Howard, T. Abzieher, I. M. Hossain, H. Eggers, F. Schackmar, S. Ternes, B. S. Richards, U. Lemmer, U. W. Paetzold, *Adv. Mater.* **2019**, 31, 1806702.
- [16] J. M. Hoffman, J. Strzalka, N. C. Flanders, I. Hadar, S. A. Cuthriell, Q. Zhang, R. D. Schaller, W. R. Dichtel, L. X. Chen, M. G. Kanatzidis, *Adv. Mater.* **2020**, 32, 2002812.
- [17] S. Lee, M. C. Tang, R. Munir, D. Barrit, Y. J. Kim, R. Kang, J. M. Yun, D. M. Smilgies, A. Amassian, D. Y. Kim, *J. Mater. Chem. A* **2020**, 8, 7695.
- [18] M. Abdelsamie, J. Xu, K. Bruening, C. J. Tassone, H. Steinrück, M. F. Toney, *Adv. Funct. Mater.* **2020**, 30, 2001752.
- [19] Y. Ju, S. Y. Park, K. M. Yeom, J. H. Noh, H. S. Jung, *ACS Appl. Mater. Interfaces* **2019**, 11, 11537.
- [20] V. Thampy, K. H. Stone, *Inorg. Chem.* **2020**, 59, 13364.
- [21] S. J. Park, A. R. Kim, J. T. Hong, J. Y. Park, S. Lee, Y. H. Ahn, *J. Phys. Chem. Lett.* **2017**, 8, 401.
- [22] G. Újvári, S. Zamini, R. Ebner, in *25th European Photovoltaic Solar Energy Conf. Exhibition/5th World Conf. on Photovoltaic Energy Conversion*, WIP GmbH & Co Planungs-KG, Valencia, Spain **2010**, p. 333.
- [23] J. J. van Franeker, K. H. Hendriks, B. J. Bruijnaers, M. W. G. M. Verhoeven, M. M. Wienk, R. A. J. Janssen, *Adv. Energy Mater.* **2017**, 7, 1601822.
- [24] C. Rehermann, A. Merdasa, K. Suchan, V. Schröder, F. Mathies, E. L. Unger, *ACS Appl. Mater. Interfaces* **2020**, 12, 30343.
- [25] K. Schötz, A. M. Askar, W. Peng, D. Seeberger, T. P. Gujar, M. Thelakkat, A. Köhler, S. Huettner, O. M. Bakr, K. Shankar, F. Panzer, *J. Mater. Chem. C* **2020**, 8, 2289.
- [26] M. Liao, B. Shan, M. Li, *J. Phys. Chem. Lett.* **2019**, 10, 1217.

- [27] M. Chauhan, Y. Zhong, K. Schötz, B. Tripathi, A. Köhler, S. Huettner, F. Panzer, *J. Mater. Chem. A* **2020**, *8*, 5086.
- [28] J. Li, A. Dobrovolsky, A. Merdasa, E. L. Unger, I. G. Scheblykin, *ACS Omega* **2018**, *3*, 14494.
- [29] M. Do, I. Kim, M. A. Kolaczowski, J. Kang, G. A. Kamat, Z. Yuan, N. S. Barchi, L. W. Wang, Y. Liu, M. J. Jurow, C. M. Sutter-Fella, *Nanoscale* **2019**, *11*, 17262.
- [30] K. Suchan, J. Just, P. Becker, E. L. Unger, T. Unold, *J. Mater. Chem. A* **2020**, *8*, 10439.
- [31] M. Buchhorn, S. Wedler, F. Panzer, *J. Phys. Chem. A* **2018**, *122*, 9115.
- [32] J. Li, R. Munir, Y. Fan, T. Niu, Y. Liu, Y. Zhong, Z. Yang, Y. Tian, B. Liu, J. Sun, D. M. Smilgies, S. Thoroddsen, A. Amassian, K. Zhao, S. (Frank) Liu, *Joule* **2018**, *2*, 1313.
- [33] H. Hu, Z. Ren, P. W. K. Fong, M. Qin, D. Liu, D. Lei, X. Lu, G. Li, *Adv. Funct. Mater.* **2019**, *29*, 1900092, <https://onlinelibrary.wiley.com/doi/full/10.1002/adfm.201900092>.
- [34] T. Trupke, B. Mitchell, J. W. Weber, W. McMillan, R. A. Bardos, R. Kroeze, *Energy Procedia* **2012**, *15*, 135.
- [35] P. Edelman, W. Henley, J. Lagowski, *Semicond. Sci. Technol.* **1992**, *7*, A22.
- [36] S. Johnston, D. Albin, P. Hacke, S. P. Harvey, H. Moutinho, C. S. Jiang, C. Xiao, A. Parikh, M. Nardone, M. Al-Jassim, W. K. Metzger, *Sol. Energy Mater. Sol. Cells* **2018**, *178*, 46.
- [37] P. Pistor, T. Hahn, T. Walter, M. Teukam, Y. Wang, F. Schönberger, T. Lavrenko, in *27th European Photovoltaic Solar Energy Conf. Exhibition*, **2012**, p. 2174.
- [38] X. Deng, X. Wen, J. Zheng, T. Young, C. F. J. Lau, J. Kim, M. Green, S. Huang, A. Ho-Baillie, *Nano Energy* **2018**, *46*, 356.
- [39] F. Zheng, W. Chen, T. Bu, K. P. Ghiggino, F. Huang, Y. Cheng, P. Tapping, T. W. Kee, B. Jia, X. Wen, *Adv. Energy Mater.* **2019**, *9*, 1901016.
- [40] Z. Hameiri, A. M. Soufiani, M. K. Juhl, L. Jiang, F. Huang, Y.-B. Cheng, H. Kampwerth, J. W. Weber, *Prog. Photovolt. Res. Appl.* **2015**, *15*, 659.
- [41] A. M. Soufiani, Z. Hameiri, S. Meyer, S. Lim, M. J. Y. Tayebjee, J. S. Yun, A. Ho-Baillie, G. J. Conibeer, L. Spiccia, M. A. Green, *Adv. Energy Mater.* **2017**, *7*, 1.
- [42] R. J. Stoddard, F. T. Eickemeyer, J. K. Katahara, H. W. Hillhouse, *J. Phys. Chem. Lett.* **2017**, *8*, 3289.
- [43] L. E. Mundt, F. D. Heinz, S. Albrecht, M. Mundus, M. Saliba, J. P. Correa-Baena, E. H. Anaraki, L. Korte, M. Gratzel, A. Hagfeldt, B. Rech, M. C. Schubert, S. W. Glunz, *IEEE J. Photovolt.* **2017**, *7*, 1081.
- [44] D. Walter, Y. Wu, T. Duong, J. Peng, L. Jiang, K. C. Fong, K. Weber, *Adv. Energy Mater.* **2018**, *8*, 1701522.
- [45] B. Schmidt-Hansberg, M. Sanyal, M. F. G. Klein, M. Pfaff, N. Schnabel, S. Jaiser, A. Vorobiev, E. Müller, A. Colsmann, P. Scharfer, D. Gerthsen, U. Lemmer, E. Barrena, W. Schabel, *ACS Nano* **2011**, *5*, 8579, <https://doi.org/10.1021/nn2036279>.
- [46] S. Ternes, T. Börnhorst, J. A. Schwenzer, I. M. Hossain, T. Abzieher, W. Mehlmann, U. Lemmer, P. Scharfer, W. Schabel, B. S. Richards, U. W. Paetzold, *Adv. Energy Mater.* **2019**, 1901581, 1901581.
- [47] F. C. Krebs, *Sol. Energy Mater. Sol. Cells* **2009**, *93*, 394.
- [48] S. K. Karunakaran, G. M. Arumugam, W. Yang, S. Ge, S. N. Khan, X. Lin, G. Yang, *J. Mater. Chem. A* **2019**, *7*, 13873.
- [49] J. E. Bishop, J. A. Smith, D. G. Lidzey, *ACS Appl. Mater. Interfaces* **2020**, *12*, 48237.
- [50] W. Sutherland, *Philos. Mag. Ser.* **2009**, *5*, 507.
- [51] K. A. Bush, N. Rolston, A. Gold-Parker, S. Manzoor, J. Hausele, Z. J. Yu, J. A. Raiford, R. Cheacharoen, Z. C. Holman, M. F. Toney, R. H. Dauskardt, M. D. McGehee, *ACS Energy Lett.* **2018**, *3*, 1225.
- [52] T. Bin Song, Z. Yuan, M. Mori, F. Motiwala, G. Segev, E. Masquelier, C. V. Stan, J. L. Slack, N. Tamura, C. M. Sutter-Fella, *Adv. Funct. Mater.* **2020**, *30*, 1908337.
- [53] D. P. Neon, J. A. Christians, L. M. Wheeler, J. L. Blackburn, E. M. Sanehira, B. Dou, M. L. Olsen, K. Zhu, J. J. Berry, J. M. Luther, *Energy Environ. Sci.* **2016**, *9*, 2072.
- [54] P. Fassel, Y. Zakharko, L. M. Falk, K. P. Goetz, F. Paulus, A. D. Taylor, J. Zaumseil, Y. Vaynzof, *J. Mater. Chem. C* **2019**, *7*, 5285.
- [55] R. Schmager, G. Gomard, B. S. Richards, U. W. Paetzold, *Sol. Energy Mater. Sol. Cells* **2019**, *192*, 65.
- [56] P. Fassel, V. Lami, F. J. Berger, L. M. Falk, J. Zaumseil, B. S. Richards, I. A. Howard, Y. Vaynzof, U. W. Paetzold, *Matter* **2021**, *4*, 1391.
- [57] M. Stolterfoht, P. Caprioglio, C. M. Wolff, J. A. Márquez, J. Nordmann, S. Zhang, D. Rothhardt, U. Hörmann, Y. Amir, A. Redinger, L. Kegelmann, F. Zu, S. Albrecht, N. Koch, T. Kirchartz, M. Saliba, T. Unold, D. Neher, *Energy Environ. Sci.* **2019**, *12*, 2778.
- [58] J. W. Lee, S. H. Bae, N. De Marco, Y. T. Hsieh, Z. Dai, Y. Yang, *Mater. Today Energy* **2018**, *7*, 149.
- [59] M. Yang, Y. Zeng, Z. Li, D. H. Kim, C. S. Jiang, J. Van De Lagemaat, K. Zhu, *Phys. Chem. Chem. Phys.* **2017**, *19*, 5043.
- [60] J. M. Richter, M. Abdi-Jalebi, A. Sadhanala, M. Tabachnyk, J. P. H. Rivett, L. M. Pazos-Outón, K. C. Gödel, M. Price, F. Deschler, R. H. Friend, *Nat. Commun.* **2016**, *7*, 1.
- [61] L. Wagner, L. E. Mundt, G. Mathiazhagan, M. Mundus, M. C. Schubert, S. Mastroianni, U. Würfel, A. Hinsch, S. W. Glunz, *Sci. Rep.* **2017**, *7*, 1.
- [62] K. P. Goetz, A. D. Taylor, F. Paulus, Y. Vaynzof, *Adv. Funct. Mater.* **2020**, *30*, 1910004.
- [63] F. Wang, S. Bai, W. Tress, A. Hagfeldt, F. Gao, *npj Flex. Electron.* **2018**, *2*, 22.
- [64] J. A. Schwenzer, L. Rakocevic, R. Gehlhaar, T. Abzieher, S. Gharibzadeh, S. Moghadamzadeh, A. Quintilla, B. S. Richards, U. Lemmer, U. W. Paetzold, *ACS Appl. Mater. Interfaces* **2018**, *10*, 16390.
- [65] C. Barugkin, J. Cong, T. Duong, S. Rahman, H. T. Nguyen, D. Macdonald, T. P. White, K. R. Catchpole, *J. Phys. Chem. Lett.* **2015**, *6*, 767.
- [66] X. Fu, J. Cong, T. Duong, H. Shen, K. J. Weber, K. R. Catchpole, T. P. White, in *Light, Energy and the Environment*, OSA Technical Digest (online) (Optical Society of America), Washington, DC **2015**, p. PTH3B.4.
- [67] X. Tang, M. Brandl, B. May, I. Levchuk, Y. Hou, M. Richter, H. Chen, S. Chen, S. Kahmann, A. Osvet, F. Maier, H. P. Steinrück, R. Hock, G. J. Matt, C. J. Brabec, *J. Mater. Chem. A* **2016**, *4*, 15896.
- [68] K. P. Goetz, A. D. Taylor, F. Paulus, Y. Vaynzof, *Adv. Funct. Mater.* **2020**, *30*, 1910004.
- [69] W. Nie, H. Tsai, R. Asadpour, A. J. Neukirch, G. Gupta, J. J. Crochet, M. Chhowalla, S. Tretiak, M. A. Alam, H. Wang, *Science* **2015**, *347*, p. 522, p. 519, <https://doi.org/10.1126/science.aaa0472>.
- [70] V. D'Innocenzo, A. R. Srimath Kandada, M. De Bastiani, M. Gandini, A. Petrozza, *J. Am. Chem. Soc.* **2014**, *136*, 17730.
- [71] Q. Zhao, A. Hazarika, L. T. Schelhas, J. Liu, E. A. Gaulding, G. Li, M. Zhang, M. F. Toney, P. C. Sercel, J. M. Luther, *ACS Energy Lett.* **2020**, *5*, 238.
- [72] S. Rahimnejad, A. Kovalenko, S. M. Forés, C. Aranda, A. Guerrero, *ChemPhysChem* **2016**, *17*, 2795.
- [73] B. Chen, J. Peng, H. Shen, T. Duong, D. Walter, S. Johnston, M. M. Al-Jassim, K. J. Weber, T. P. White, K. R. Catchpole, D. Macdonald, H. T. Nguyen, *Adv. Energy Mater.* **2018**, *9*, 1802790.
- [74] S. D. Stranks, V. M. Burlakov, T. Leijtens, J. M. Ball, A. Goriely, H. J. Snaith, *Phys. Rev. Appl.* **2014**, *2*, 034007.